nature catalysis

Article

https://doi.org/10.1038/s41929-022-00880-6

Copper/alkaline earth metal oxide interfaces for electrochemical CO_2-to-alcohol conversion by selective hydrogenation

Received: 23 October 2020

Accepted: 13 October 2022

Published online: 24 November 2022

Check for updates

Aoni Xu[1,2,3,8], Sung-Fu Hung[1,4,8], Ang Cao[3,8], Zhenbin Wang[3,8], Naiwrit Karmodak[3], Jianan Erick Huang[1], Yu Yan[1], Armin Sedighian Rasouli[1], Adnan Ozden[5], Feng-Yi Wu[4], Zih-Yi Lin[4], Hsin-Jung Tsai[4], Tsung-Ju Lee[4], Fengwang Li[1], Mingchuan Luo[1], Yuhang Wang[1], Xue Wang[1], Jehad Abed[1,6], Ziyun Wang[1], Dae-Hyun Nam[1], Yuguang C. Li[1,7], Alexander H. Ip[1], David Sinton[5], Chaofang Dong[2] ✉ & Edward H. Sargent[1] ✉

Multicarbon alcohols produced by electrochemical CO_2 reduction (CO_2RR) are attractive alternatives to fossil fuels; however, the selectivity towards alcohols in CO_2RR remains low, a result of competing hydrocarbon (that is, ethylene) production. Here we report on Cu catalysts decorated with different alkaline earth metal oxides (MOs). We found that BaO delivers a Faradaic efficiency of 61% towards C_{2+} alcohols. At an industry-relevant current density of 400 mA cm^{-2}, the ratio of alcohols to hydrocarbon reached 3:1. Mechanistic studies, including in operando X-ray absorption spectroscopy, in situ Raman spectroscopy and density functional theory calculations, suggested that the increased selectivity towards alcohols originates from sites at the MO/Cu interface. Furthermore, computational studies indicated that the incorporation of MOs favours a hydroxy-containing C_2 intermediate (*HCCHOH) over the hydrocarbon intermediate (*HCC) at interfacial Cu sites on the path to alcohol products. We also propose that the relative bond strengths of Cu–COH and C–OH correlate with the selectivity for alcohol over hydrocarbon.

The electrocatalytic reduction of CO_2 (CO_2RR) to valuable fuels and feedstocks using renewable electricity presents a carbon-neutral route to fuel generation[1,2]. Among multicarbon CO_2RR products, ethanol and *n*-propanol are particularly desired to replace fossil fuels owing to their high volumetric energy density and compatibility with existing storage and transportation infrastructure[3–5].

Recent studies have revealed that the alcohol yield can be increased by improving the C–C coupling process[6], achieved through diverse surface binding sites[7], a CO-rich local environment[8], metal–support interactions[9] and cooperative promotion at multiple sites[10]. However, control of alcohol selectivity over hydrocarbon selectivity remains a challenge, with a Faradaic efficiency

[1]Department of Electrical and Computer Engineering, University of Toronto, Toronto, Ontario, Canada. [2]Beijing Advanced Innovation Center for Materials Genome Engineering, Institute for Advanced Materials and Technology, University of Science and Technology Beijing, Beijing, China. [3]Catalysis Theory Center, Department of Physics, Technical University of Denmark, Lyngby, Denmark. [4]Department of Applied Chemistry, National Yang Ming Chiao Tung University, Hsinchu, Taiwan. [5]Department of Mechanical and Industrial Engineering, University of Toronto, Toronto, Ontario, Canada. [6]Department of Materials Science and Engineering, University of Toronto, Toronto, Ontario, Canada. [7]Department of Chemistry, University at Buffalo, Buffalo, NY, USA. [8]These authors contributed equally: Aoni Xu, Sung-Fu Hung, Ang Cao, Zhenbin Wang. ✉e-mail: cfdong@ustb.edu.cn; ted.sargent@utoronto.ca

https://doi.org/10.1038/s41929-022-00880-6

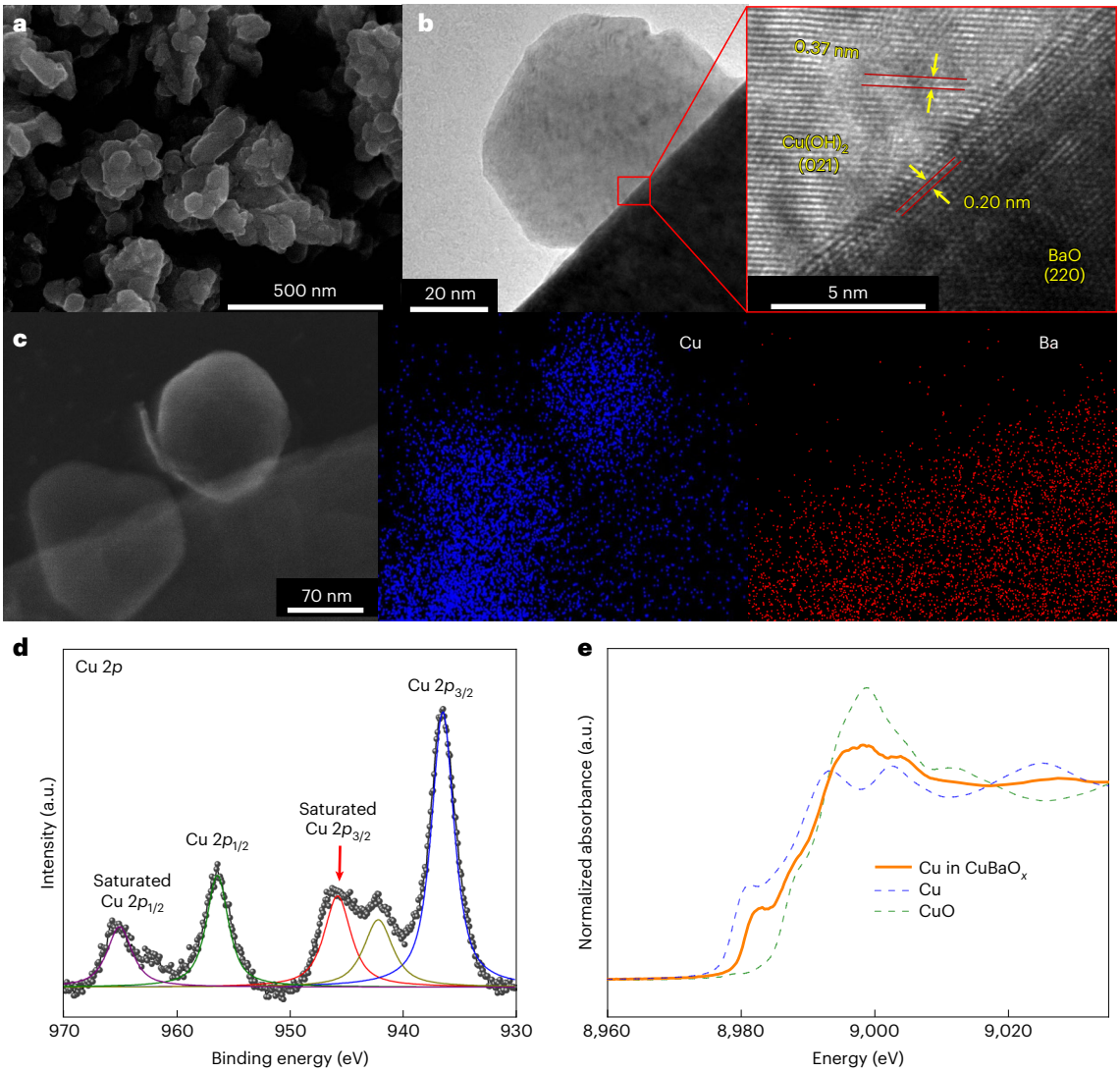

Fig. 1 | Characterization of the as-prepared BaO/Cu electrocatalysts. a,**b**, SEM (**a**) and HRTEM (**b**) images of the precursor hydroxide composites of the BaO/Cu catalyst. The right-hand image in b shows a magnified image of the highlighted red square, revealing the interfacial structure in detail. **c**, STEM image (left) and the corresponding EDX mapping images (Cu and Ba) of the precursor hydroxide composites of the BaO/Cu catalyst. **d**, XPS spectrum of Cu 2*p*, showing that both Cu and Cu(II) are present in the sample. **e**, XANES spectra of the Cu K-edge of Cu, CuO and the as-prepared BaO/Cu catalyst.

(FE) towards alcohol products of less than 54% having previously been reported[11].

Oxidized copper facilitates the conversion of CO_2 into oxygenates, for example, methanol[12], ethanol[13,14] and oxalate[15], by suppressing hydrocarbon products, and has achieved 99% selectivity towards ethanol in thermocatalysis[16]. However, oxidized Cu is reduced under electrochemical CO_2RR conditions, and this impedes its use in alcohol production. In light of recent in situ studies[14,17–20] of interface reactions between Cu and metal oxides, we posited that the oxidized state of Cu could be stabilized at the interface between Cu and a metal oxide under CO_2RR conditions.

In this study we introduced a series of alkaline earth metal oxides (MOs)—in which the metal elements maintain their oxidation states up to −2 V versus the standard hydrogen electrode (SHE)—onto Cu to fabricate robust MO/Cu interfaces. In a gas diffusion electrode-based flow-cell system, these MO/Cu catalysts achieved 2–2.5 times greater selectivity over hydrocarbons (FE ratio of ~3:1) compared with pure Cu. In operando X-ray absorption spectroscopic analysis suggested that interfacial Cu sites are partially oxidized by the MOs. Density functional theory (DFT) calculations revealed that the partially positively charged Cu sites weaken the Cu–COH bond of a *HCCOH intermediate, facilitating hydrogenation at the C atom, thereby preserving the OH group and favouring alcohol production.

Results

MO/Cu catalysts promote CO_2-to-alcohol conversion over hydrocarbon

To construct MO/Cu catalysts experimentally, we incorporated MOs (M = Ba, Sr and Ca) into Cu through a co-precipitation method. The addition of aqueous alkali to a mixed alkaline earth metal and Cu salt solution under stirring led to the co-precipitation of mixed-metal material (see Methods). As shown in Supplementary Fig. 1, X-ray diffraction analysis of this precursor material prepared with $Ba(NO_3)_2$ revealed a mixture of crystalline $Cu(OH)_2$ and BaO (hydrate), as expected from a co-precipitation method[21]. Scanning electron microscopy (SEM) of the mixed catalysts revealed nanoparticles on the scale of tens of nanometres with well-defined interfacial boundaries (Fig. 1a). High-resolution transmission electron microscopy (HRTEM) showed lattice fringes of BaO and $Cu(OH)_2$ in different particle domains, with the lattice parameters of 0.37 and 0.20 nm matching well those of $Cu(OH)_2$ and BaO

https://doi.org/10.1038/s41929-022-00880-6

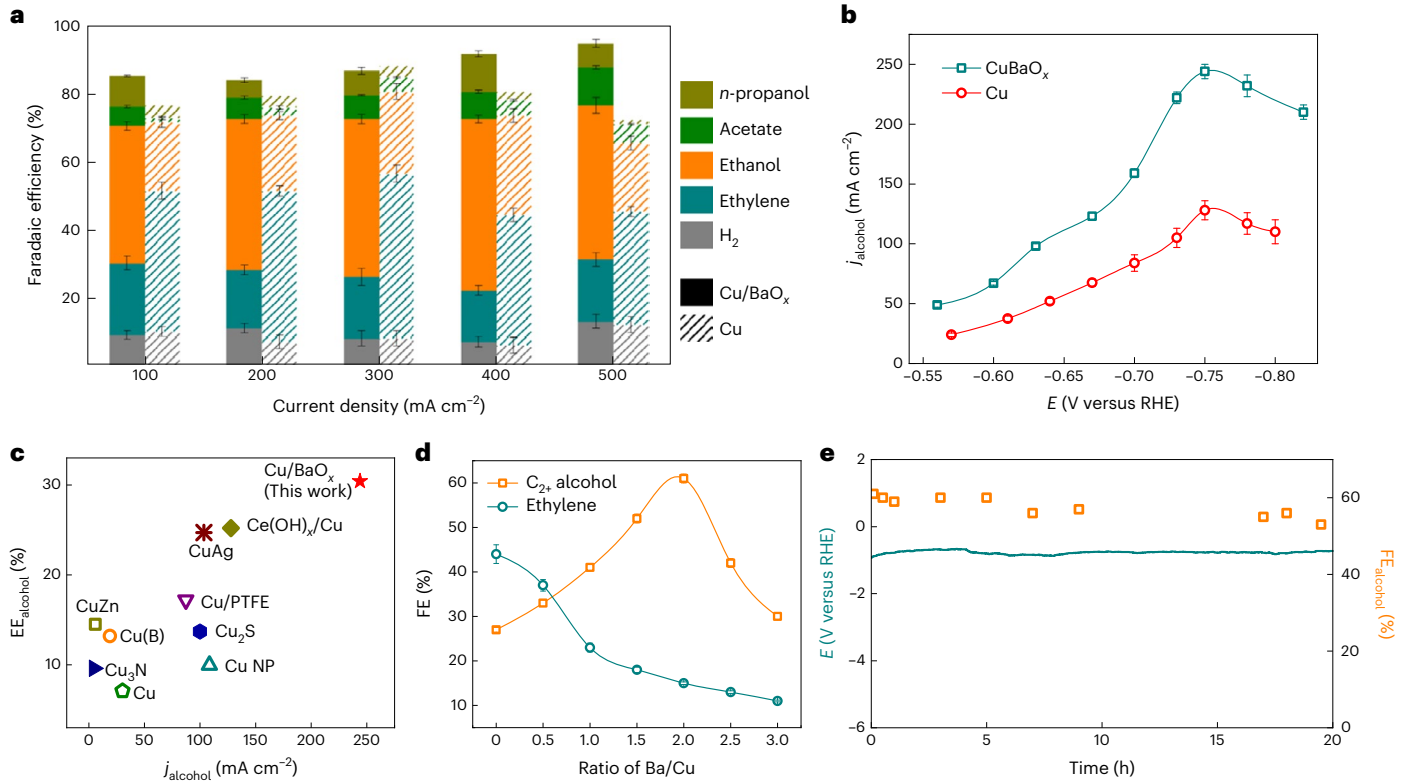

Fig. 2 | CO_2RR performance of the BaO/Cu catalyst. a, CO_2RR product distribution obtained with the BaO/Cu and Cu catalysts at various current densities in 1 M KOH. **b**, Variation in the partial current densities of C_{2+} alcohols with potential with the BaO/Cu and Cu catalysts. **c**, Comparison of the energy efficiency and partial current density for CO_2-to-alcohol conversion determined in this work and in previous studies. NP, nanoparticles. **d**, Comparison of alcohol and ethylene selectivity on BaO/Cu catalysts fabricated with various concentrations of Ba (in the precursor). **e**, Stability of the BaO/Cu catalyst at a constant applied current density of 400 mA cm^{-2} and the corresponding alcohol FE. The error bars represent the mean ± SD ($n = 3$ replicates).

(Fig. 1b). Scanning transmission electron microscopy (STEM) with energy-dispersive X-ray spectroscopy (EDX) mapping further confirmed the phase separation of $Cu(OH)_2$ and BaO (Fig. 1c and Supplementary Fig. 2). The oxidation states of Cu and Ba in these mixtures were determined by high-resolution X-ray photoelectron spectroscopy (XPS; Fig. 1d and Supplementary Fig. 3). X-ray absorption near-edge structure (XANES) analysis of the Cu K-edge (Fig. 1e) further confirmed that Cu has an average oxidation state of +1.96 ± 0.01 in the mixed catalyst.

We then sprayed these nanoparticles onto a porous polytetrafluoroethylene (PTFE) substrate and assessed the CO_2RR performance in a flow cell using 1 M KOH as the electrolyte (Supplementary Fig. 4). The precursor material was reduced immediately, forming BaO/Cu. The catalyst exhibited twofold increased selectivity for alcohol products (ethanol and *n*-propanol) compared with pure Cu: this remained the case over a range of applied current densities spanning from 100 to 500 mA cm^{-2} (Fig. 2a). An FE of 61% towards C_{2+} alcohols was achieved with a partial current density of 244 mA cm^{-2} (Fig. 2b). The half-cell energy efficiency for CO_2-to-alcohol conversion was 30%. Comparison with the literature showed that both the alcohol partial current density and the energy efficiency were higher than those reported previously[6,7,10,22–24] (Fig. 2c). The selectivity for alcohols increased with Ba concentration until the molar ratio of Ba and Cu reached ~2:1 (Fig. 2d); the FE towards C_{2+} was observed to decrease on further increasing the Ba content, which we attribute to a lack of available Cu sites. At a current density of 400 mA cm^{-2}, the system operated at a stable potential of −0.75 V versus the reversible hydrogen electrode (RHE) and delivered a stable alcohol FE of 58% over 20 h of continuous operation (Fig. 2e).

Similar electrocatalytic behaviour was observed when we replaced BaO in the Cu/MO catalyst with CaO or SrO (Supplementary Figs. 5 and 6): the production of ethanol and *n*-propanol increased with a total FE of 46% for CaO/Cu and 49% for SrO/Cu, compared with an FE of 23% on pure Cu.

Interfacial Cu sites stabilize hydroxy-containing intermediates

We further assessed the stability of this catalytic system using in situ spectroscopic techniques. We first carried out in operando X-ray absorption spectroscopy (XAS) in a flow cell to determine the chemical states of Cu and Ba under CO_2RR conditions. At a constant current density of 400 mA cm^{-2}, the Cu species were partially reduced within 3 min and then maintained a steady oxidation state, which we estimated by Cu K-edge XANES analysis to average ~0.7–0.9 (Fig. 3a,b, evaluated using a linear relationship of the edge shift[25], and Supplementary Figs. 7 and 8), whereas the pure copper oxide/hydroxide system was reduced rapidly to the metallic state[26]. We further conducted linear combination fitting of the XANES spectra to calculate the composition of Cu, finding a mixture of Cu^0 (44%), Cu_2O (18%), CuO (1%) and $Cu(OH)_2$ (37%; Supplementary Fig. 9). We tentatively ascribed these results to the abundant Cu/BaO interfaces giving rise to a rearrangement of electrons between Cu and the oxide[27–30]. Real-time Cu K-edge extended X-ray absorption fine structure (EXAFS) spectroscopy further confirmed the existence of Cu–O bonds during the CO_2RR (Supplementary Fig. 11). Furthermore, Ba L_3-edge XANES spectroscopy (Supplementary Fig. 12) showed that Ba remained in the +2 oxidation state during CO_2RR up to an applied potential of −1.58 V versus RHE.

We then performed in situ Raman measurements across a potential range from −0.24 to −0.73 V versus RHE to explore the adsorption behaviour of the chemical intermediates at the active sites. The Raman spectra in Fig. 3c,d show four different Raman bands related to the *CO intermediate at 280, 360, 2,040 and 2,080 cm^{-1} for both the

https://doi.org/10.1038/s41929-022-00880-6

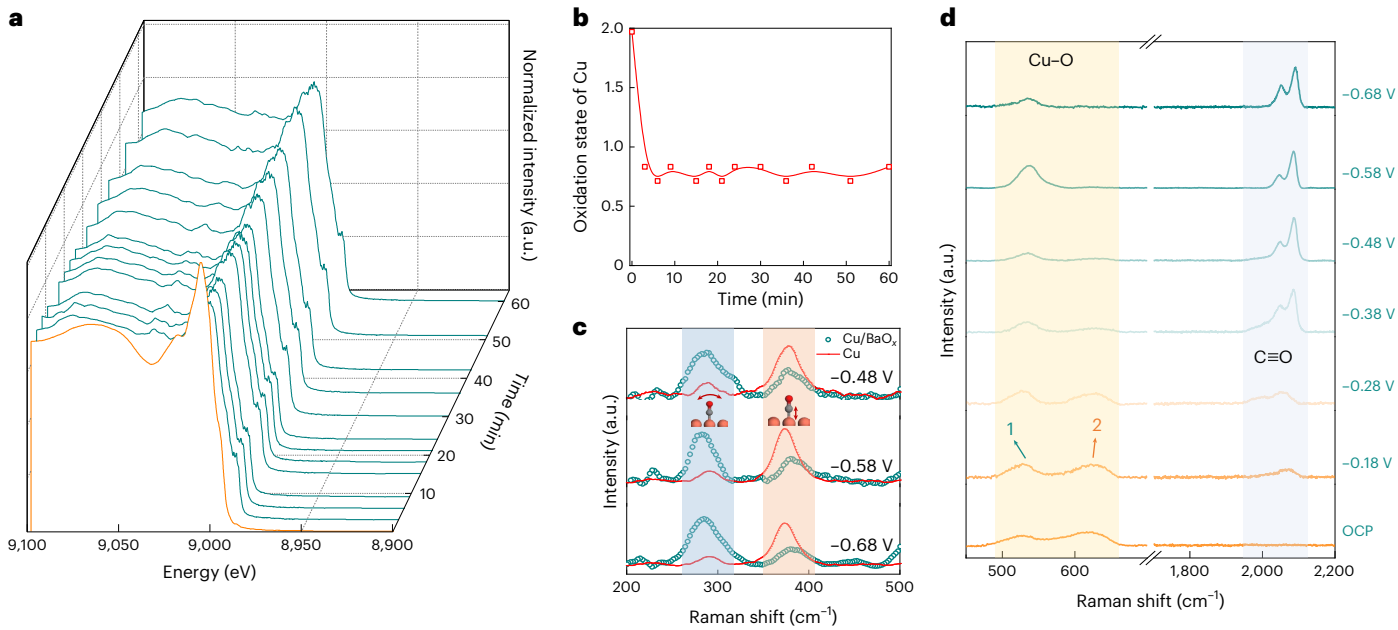

Fig. 3 | Surface states of the BaO/Cu catalyst under CO_2RR conditions. a, Real-time XANES spectra of the Cu K-edge of the BaO/Cu catalyst at 400 mA cm^{-2} recorded over a period of 1 h. The orange curve represents the XANES spectrum of a dry sample, and the cyan curves represent in operando spectra. **b**, Variation in the average oxidation state of Cu in the BaO/Cu catalyst with time. **c**, In situ surface-enhanced Raman spectra of the BaO/Cu and pure copper catalysts in the range 200–500 cm^{-1} at different applied potentials (versus RHE, where OCP is the open circuit potential). **d**, Raman spectra of the BaO/Cu catalyst in the range 450–2,200 cm^{-1} at different applied potentials (versus RHE). Peaks 1 and 2 in the range 500–700 cm^{-1} correspond to Cu–O bands. All measurements were performed in 1 M KOH electrolyte.

Cu/BaO and pure Cu catalysts. For the Cu–C≡O configuration, the relative amplitudes of the rotation (280 cm^{-1}) and stretching (360 cm^{-1}) bands of Cu–CO[31–33] are reversed for the Cu/BaO (Fig. 3c) and pure Cu catalysts. Furthermore, the C≡O stretching bands are deconvoluted into two bands at 2,040 cm^{-1} (ref. [34]) and 2,080 cm^{-1} (Fig. 3d), with the low-frequency band being less prominent with the pure Cu catalyst (Supplementary Fig. 12). The new low-frequency C≡O stretching band for Cu/BaO has been assigned to a dynamic CO intermediate that contributes to the ensuing C–C coupling[34]. The relative intensities of the low- and high-frequency bands of the different catalysts were further analysed (Supplementary Figs. 13–15), with BaO/Cu showing the highest ratio (0.57). A linear relationship was found between C_{2+} selectivity and the relative intensity (Supplementary Fig. 16), indicating the contribution of the low-frequency band to C_{2+} production. The blueshift of the CC (in ethanol) stretching band[35] on BaO/Cu (1,032 cm^{-1}, Supplementary Fig. 17) attests to the stabilization of C_2 intermediates on this catalyst. We ascribe the high-frequency stretching band to an isolated and static CO adsorbate, with a rising intensity at higher overpotentials, in agreement with the decreasing C_2 selectivity at more cathodic potentials (Fig. 2b).

We observed two peaks related to Cu–O bands in the Raman spectra (Fig. 3d): peak 1 above 500 cm^{-1} corresponds to the T_{2g} vibrational mode of Cu_2O (refs. [33,36]) and $Cu(OH)_2$ (ref. [37]), whereas peak 2 above 600 cm^{-1} arises from the B_g mode of CuO (refs. [38,39]). The Raman spectra show that the intensity of peak 2 is dependent on the potential: as the potential becomes more negative, peak 2 gradually decreases and even disappears beyond −0.38 V, suggesting a charge-transfer conversion from CuO (peak 2) to Cu_2O (peak 1) or pure Cu (no Cu–O band) in the BaO/Cu catalyst. This observation is consistent with the in situ XANES analysis (Supplementary Fig. 9), in which only 1% CuO was detected under CO_2RR conditions. Interestingly, when peak 1 starts to grow and becomes the dominant Cu–O band (at −0.38 V), C≡O stretching bands also appear and split. Comparing with pure Cu (Supplementary Fig. 12), we assign the Cu–C≡O configuration (Fig. 3d) to newly formed Cu sites (metallic and partially oxidized Cu) on BaO/Cu.

To explore in silico the possible role of the active Cu sites on BaO/Cu in alcohol selectivity, we first sought to identify a leading candidate for the model of the catalyst surface. We used an approach informed by previous studies of metal oxide catalysts[40–45], one that seeks to capture the influence of the oxide at the interface without adding more variables than is necessary.

We screened a series of Cu and BaO interfaces based on their geometric mismatch (Supplementary Table 1) and formation energies (Supplementary Figs. 18 and 19 and Supplementary Table 2). This led us to use BaO(111)/Cu(111) (Supplementary Fig. 20) to represent the BaO/Cu interface, as it has the lowest formation energy and lattice mismatch.

We investigated the electronic influence of BaO on the interfacial Cu sites. As shown in Fig. 4a, the incorporation of BaO induces a rearrangement of the electrons in the interfacial Cu atoms, giving rise to positively charged Cu sites, consistent with the in operando XANES analysis (Fig. 3b).

This interfacial model was then used to investigate the CO_2RR at both interfacial Cu and metallic Cu sites. The data presented in Fig. 2a indicate that the BaO/Cu catalyst shows a higher alcohol selectivity but a similar total FE towards C_{2+} products compared with Cu alone. Previous mechanistic studies[46,47] suggested that the C_2 products ethylene and ethanol share similar initial reaction pathways: they both begin with *CO dimerization, but they diverge from *HCCOH. The proton–electron transfer step, in which *HCCOH progresses to a hydrocarbon intermediate (*HCC) or a hydroxy-containing intermediate (*HCCHOH), is the branching point for ethylene versus ethanol formation. We therefore calculated the reaction energies of the conversions of *HOCCH to *HCC (ethylene pathway) and *HOCCH to *HOCHCH (ethanol pathway) to investigate the effect of BaO on the C_2 product distribution.

Compared with bare Cu, the interfacial Cu sites in the BaO(111)/Cu(111) model promote the hydrogenation of *HCCOH to both hydrocarbon and hydroxy-containing intermediates, lowering the reaction energies by 0.25 and 0.45 eV, respectively (Fig. 4b), while Cu sites remote from BaO show similar adsorption features to that of bare Cu (Supplementary Fig. 21). The preference for *HCCHOH over *HCC at

https://doi.org/10.1038/s41929-022-00880-6

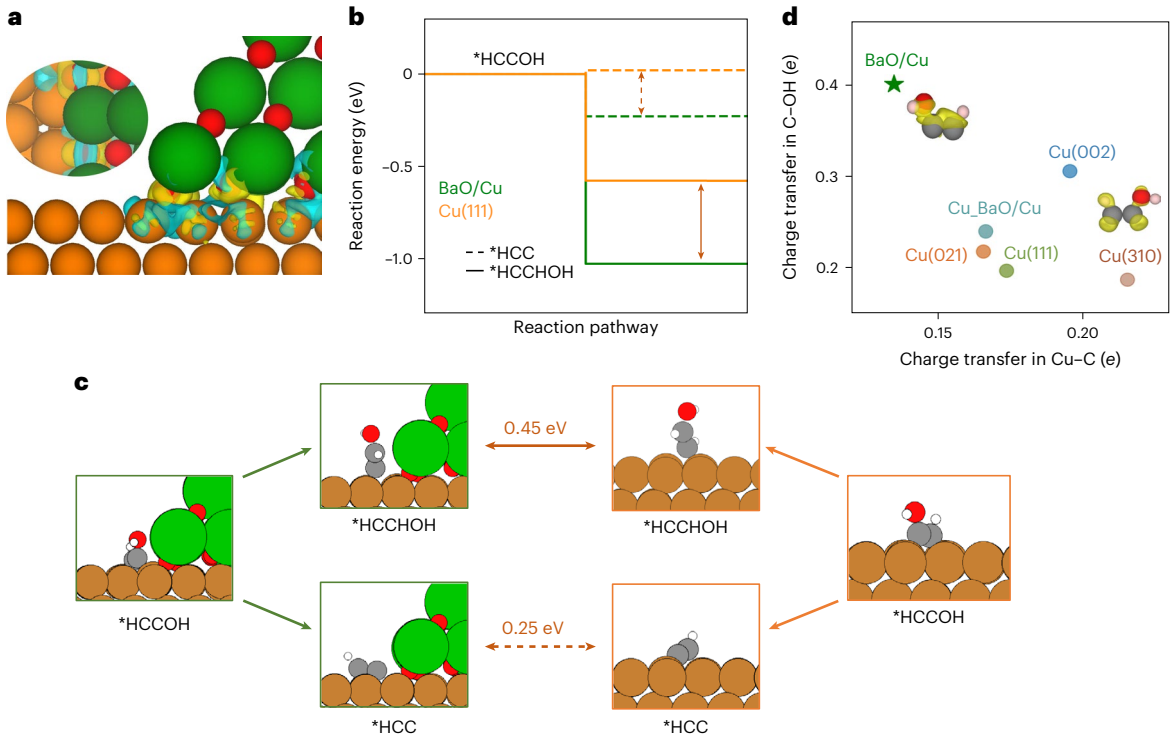

Fig. 4 | DFT calculations of hydrogenation reactions and design principle. **a**, Charge density difference in the BaO(111)/Cu(111) model. Yellow and blue contours represent the isosurfaces of electronic charge accumulation and depletion, respectively, indicating that electrons transfer from the interfacial Cu sites to the adjacent O atoms. **b**, Reaction energy diagram for the hydrogenation (*HCCOH + H_2O + e^- → *HCCHOH + OH^-) and dehydroxylation (*HCCOH + e^- → *HCC + OH^-) steps on BaO(111)/Cu(111) and Cu(111). **c**, Configurations of *HCCOH on BaO(111)/Cu(111) (left) and Cu(111) (right) in the different reaction path. The adsorption energy of *HCCHOH on BaO(111)/Cu(111) is 0.45 eV lower than on Cu(111), whereas the adsorption energy of *HCC is lower by 0.25 eV. **d**, Charge transfer in C–OH and Cu–COH in *HCCOH adsorbed on different catalyst models, where BaO/Cu and Cu_BaO/Cu represent the interfacial and non-interfacial Cu sites in the BaO/Cu model, respectively.

interfacial Cu sites (Fig. 4c) offers one explanation for the experimentally observed improved selectivity for alcohols on BaO/Cu.

Inspecting the hydrogenation and dehydroxylation steps, we note that the former (*HCCOH + H_2O + e^- → *HCCHOH + OH^-) leads to the rupture of the **Cu–C**OH bond and the formation of a C–H bond, while the dehydroxylation step (*HCCOH + e^- → *HCC + OH^-) requires cleavage of the C–OH bond. We posit the relative bond strength of Cu–COH compared with C–OH in *HCCOH as a descriptor for alcohol selectivity. We used Bader charge density analysis to quantify the charge transfer in Cu–COH and C–OH as a surrogate for bond strength. As shown in Fig. 4d, the interfacial Cu sites of the BaO/Cu catalyst evidence more charge transfer from C to the OH group and less charge transfer between Cu and C atoms, indicating stronger C–OH and weaker Cu–COH bonds.

In previous studies, alcohol selectivity was reported on catalysts that create asymmetric sites[7] and introduce confinement effects[11]. Analysing the results of these previous studies and the present work, we propose that, to favour hydroxy group conservation and thus the production of alcohols, one must seek to weaken the relative strength of the Cu–COH interaction by material modification strategies, for example, by breaking the compact and well-ordered surface structure of Cu (asymmetry strategy), donating electrons to COH from the nitrogen-doped carbon (N–C) layer (confinement strategy), and decorating and stabilizing strongly electronegative elements to extract electrons from Cu (constructing Cu/oxide interfaces).

Discussion

In summary, we have found that the decoration of Cu with MOs promotes CO_2-to-alcohol conversion. In particular, BaO/Cu delivered a 2.5-fold higher alcohol selectivity than pure Cu by suppressing hydrocarbon production. The enhanced alcohol selectivity is ascribed to the newly formed interfacial Cu sites that stabilize the hydroxy-containing C_2 intermediates. We also explored, as a descriptor of alcohol selectivity, the bond strength of Cu–COH: weakening the Cu–COH bond favours the hydrogenation of the C atom over the O atom, preserving the OH group, thereby accounting for the increased yield of alcohol. This descriptor rationalizes different catalyst design strategies reported in the literature for enhancing alcohol selectivity. Beyond catalyst modification, we have also noted in recent reports that the interactions between active sites and adsorbed intermediates can also be optimized by electrolyte (for example, anion[48] or cation[49]) effects. Our finding of the alcohol selectivity descriptor could enable improvements in catalyst design towards high alcohol selectivity.

Methods

Electrode preparation

All reagents were purchased from Sigma Aldrich and used without further purification. Barium solutions were prepared by dissolving 0, 15, 30 and 45 g $Ba(NO_3)_2$ in 500 ml deionized water. Next, 0.7 g $CuCl_2$ was dissolved in 30.0 ml of the above solutions to synthesize mixed salt solutions with different Ba concentrations. Then, 30 ml of 1.0 M KOH was added dropwise to these solutions with stirring, leading to the co-precipitation of mixed-metal materials. These mixed-metal materials were rinsed with water, centrifuged three times, first with water and then with methanol, and finally dried overnight under vacuum at room temperature. PTFE electrodes were prepared by airbrushing (using N_2 as the carrier gas): precatalyst ink comprising 30 mg of as-made oxide precatalyst, 3 ml methanol and 120 µl Nafion solution (~5 wt%) was sprayed onto commercial PTFE (5 cm × 5 cm). The areal loading was ~1 mg cm^{-2}. After vacuum drying, a 2 cm × 2 cm catalyst/PTFE electrode was cut and assembled into a flow-cell electrolyser.

Material characterization

The morphology of the electrodes was characterized using a scanning electron microscope (Hitachi S-5200) with a beam voltage of 5 kV. HRTEM and elemental mapping images were collected using a Hitachi HF-3300 microscope, with an acceleration voltage of 300 kV, equipped with a Bruker EDX detector (Bruker 6 | 60 EDX detector). The the EDX studies were performed with an acquisition time of 3 min. Powder X-ray diffraction patterns were recorded using a Bruker D8 diffractometer with Cu Kα radiation (λ = 0.15406 nm). XPS was conducted on a PHI 5700 ESCA system using Al Kα X-ray radiation (1,486.6 eV) for excitation. In operando XAS investigations were carried out at the 9BM beamline of the Advanced Photon Source (APS) located in the Argonne National Laboratory. The same conditions as used in the electrochemical characterization were ensured in a specially designed flow-cell reactor with a window sealed with Kepton tape[26]. The XAS signals were collected in total-fluorescence-yield fly-scan mode for Cu K-edge measurements and in normal-scan mode for Ba L_3-edge measurements using a Vortex detector. Scans were performed in the energy range of 8,700–9,500 eV for Cu K-edge and in the range of 5,100–5,500 eV for Ba L_3-edge. The spectra were obtained by subtracting the baseline of the pre-edge and normalizing that of the post-edge. EXAFS analysis was conducted using Fourier transforms of k^3-weighted EXAFS oscillations to evaluate the contribution of each bond pair to the Fourier transform peak. Cu oxidation states were determined from the linear relationship of the edge shift in the XANES spectra. Cu foil, Cu_2O, CuO and $Cu(OH)_2$ were used as the standard samples of Cu^0, Cu^+ and Cu^{2+}. The absorption edge positions were determined from the first maximum of the first-derivative spectra, constructing a correlation between the Cu oxidation state and the energy. The sample composition during the CO_2RR was obtained by linear combination fitting of the XANES spectra using the Athena software. The fitting range was −20 to 30 eV. In situ Raman measurements were conducted on a Renishaw inVia Raman microscope with a water immersion objective (×63), a 785 nm laser and a modified flow cell using an integration time of 5 s and an average of 20 scans per region. In the above systems, a platinum wire and a Ag/AgCl electrode were used as the counter and reference electrodes, respectively.

Electrochemical measurements

Electrochemical studies were carried out using an electrochemical flow cell consisting of a gas chamber, a cathodic chamber and an anodic chamber. The PTFE-based working electrode was fixed between the gas and cathodic chambers, with the catalyst layer facing the cathodic chamber (geometric active surface area of 1 cm^2). An anion exchange membrane (Fumasep, FAA-3-PK-130) was used to separate the anodic and cathodic chambers. All electrochemical tests were conducted on an Autolab PGSTAT204 instrument, with a Ag/AgCl electrode and Ni foam as the reference and counter electrodes, respectively. Potentials were converted to the RHE scale after *iR* correction. For performance studies, 1 M KOH was used as the electrolyte, and was circulated through the cathodic and anodic chambers at a constant flow rate of 10 ml min^{-1} using peristaltic pumps. The flow rate of CO_2 gas through the gas chamber was kept constant at 50 cm^3 min^{-1} using a digital gas flow controller. A gas chromatograph (PerkinElmer Clarus 600) equipped with a flame ionization detector and a thermal conductivity detector was used to analyse the gas products collected from the outlet of the gas chamber. ^{1}H NMR spectroscopy (600 MHz, Agilent DD2 NMR spectrometer) with water suppression was used to analyse the liquid products using D_2O and dimethylsulfoxide as the lock solvent and internal reference, respectively.

DFT calculations

DFT calculations were performed with the Vienna Ab initio Simulation Package (VASP) code[50,51] using a similar set-up to our previous work[52]. The exchange correlation energy was modelled using the Perdew–Burke–Ernzerhof (PBE) functional within the generalized gradient approximation[53]. Projector augmented-wave pseudo-potentials[54] were used to describe ionic cores. The cut-off energy of 450 eV was adopted after a series of tests. A Methfessel–Paxton smearing of 0.05 eV was applied to the orbital occupation during geometry optimization and the total energy computations. In all calculations, the atoms at all positions had Hellmann–Feynman forces less than 0.05 eV $Å^{-1}$ and the electronic iteration convergence was 10^{-5} eV using the normal algorithm. We calculated the surface energies for different facets of Cu and BaO (Supplementary Table 3). The crystal structure data for the different facets of Cu and BaO are shown in Supplementary Table 4. Different interface models were built to simulate the Cu/BaO structure, with the configurations shown in Supplementary Figs. 18 and 19. The adsorption of reaction intermediates was simulated by constructing adsorption models of *HCCOH, *HCC and *HCCHOH on the BaO(111)/Cu(111) and Cu(111) models, with the configurations shown in Supplementary Figs. 22–24. During the adsorption simulations, the bottom two layers were fixed in the tested lattice positions while other layers, including adsorbates, were relaxed. Reaction energies were calculated on the basis of the computational hydrogen electrode model[55]. Solvent effects were included by using an implicit model, VASPsol[56,57]. The dielectric constant for water was set to a relative permittivity of 78.4. The Debye length for the electrolyte was set to 3.0 Å, which corresponds to an electrolyte concentration of 1.0 M. The effective surface tension was set to 0.525 meV $Å^{-2}$. The differences between the implicit and explicit models on the Cu(111) surface are shown in Supplementary Table 5. We calculated the transition state of CO dimerization using the climbing image nudged elastic band (CI-NEB) method with a string constant of −5 eV $Å^{-2}$. The energy plot generated by the CI-NEB method is shown in Supplementary Fig. 25. The configuration of the *OCCO transition state is shown in Supplementary Fig. 26, and the coordinates of all models calculated using the CI-NEB method can be found in the public GitHub repository in the data availability statement. The vibrational frequencies of the transition state are shown in Supplementary Table 6; it should be noted that there is only one imaginary frequency. We calculated the energy barrier for *OCCO for a constant potential at −0.75 V versus RHE (−1.6 V versus SHE) in the potential range of −0.55 to −0.8 V versus RHE, the range used for experimental testing (shown in Fig. 2b). The potential U was estimated according to the following equation:

$$U = \frac{-\varepsilon_F - \phi_{SHE}}{e} \quad (1)$$

where ε_F is the Fermi energy of the system and ϕ_{SHE} is the thermodynamic work function of the SHE, which is around −4.30 eV for the PBE functional, e is charge of one electron[58]. We tested the calculated potential of zero charge on different facets of Cu using this set-up (Supplementary Table 7). The Bader charge was calculated using the Bader Charge Analysis script written by Henkelman and co-workers[59]. The charge transfer in C–OH and Cu–C in the *HCCOH intermediate on Cu and Cu/BaO is summarized in Supplementary Table 8.

Data availability

All data can be found in the public GitHub repository (https://github.com/onealshu/CO2_alcohol_BaOCu.git) or from the corresponding authors upon reasonable request.

References

1. Ross, M. B. et al. Designing materials for electrochemical carbon dioxide recycling. *Nat. Catal.* **2**, 648–658 (2019).
2. Birdja, Y. Y. et al. Advances and challenges in understanding the electrocatalytic conversion of carbon dioxide to fuels. *Nat. Energy* **4**, 732–745 (2019).
3. Shih, C. F., Zhang, T., Li, J. & Bai, C. Powering the future with liquid sunshine. *Joule* **2**, 1925–1949 (2018).

4. Spurgeon, J. M. & Kumar, B. A comparative technoeconomic analysis of pathways for commercial electrochemical CO_2 reduction to liquid products. *Energy Environ. Sci.* **11**, 1536–1551 (2018).
5. Nitopi, S. et al. Progress and perspectives of electrochemical CO_2 reduction on copper in aqueous electrolyte. *Chem. Rev.* **119**, 7610–7672 (2019).
6. Zhuang, T.-T. et al. Steering post-C–C coupling selectivity enables high efficiency electroreduction of carbon dioxide to multi-carbon alcohols. *Nat. Catal.* **1**, 421–428 (2018).
7. Li, Y. C. et al. Binding site diversity promotes CO_2 electroreduction to ethanol. *J. Am. Chem. Soc.* **141**, 8584–8591 (2019).
8. Li, F. et al. Cooperative CO_2-to-ethanol conversion via enriched intermediates at molecule–metal catalyst interfaces. *Nat. Catal.* **3**, 75–82 (2020).
9. Parastaev, A. et al. Boosting CO_2 hydrogenation via size-dependent metal–support interactions in cobalt/ceria-based catalysts. *Nat. Catal.* **3**, 526–533 (2020).
10. Luo, M. et al. Hydroxide promotes carbon dioxide electroreduction to ethanol on copper via tuning of adsorbed hydrogen. *Nat. Commun.* **10**, 5814 (2019).
11. Wang, X. et al. Efficient electrically powered CO_2-to-ethanol via suppression of deoxygenation. *Nat. Energy* **5**, 478–486 (2020).
12. Le, M. et al. Electrochemical reduction of CO_2 to CH_3OH at copper oxide surfaces. *J. Electrochem. Soc.* **158**, E45 (2011).
13. Lin, S.-C. et al. Operando time-resolved X-ray absorption spectroscopy reveals the chemical nature enabling highly selective CO_2 reduction. *Nat. Commun.* **11**, 3525 (2020).
14. Gong, J. et al. Synthesis of ethanol via syngas on Cu/SiO_2 catalysts with balanced Cu^0–Cu^+ sites. *J. Am. Chem. Soc.* **134**, 13922–13925 (2012).
15. Angamuthu, R., Byers, P., Lutz, M., Spek, A. L. & Bouwman, E. Electrocatalytic CO_2 conversion to oxalate by a copper complex. *Science* **327**, 313–315 (2010).
16. An, B. et al. Cooperative copper centres in a metal–organic framework for selective conversion of CO^2 to ethanol. *Nat. Catal.* **2**, 709–717 (2019).
17. Wang, Z.-Q. et al. High-performance and long-lived Cu/SiO_2 nanocatalyst for CO_2 hydrogenation. *ACS Catal.* **5**, 4255–4259 (2015).
18. Dong, X. et al. CO_2 hydrogenation to methanol over $Cu/ZnO/ZrO_2$ catalysts prepared by precipitation-reduction method. *Appl. Catal. B* **191**, 8–17 (2016).
19. Chu, S. et al. Stabilization of Cu^+ by tuning a CuO–CeO_2 interface for selective electrochemical CO_2 reduction to ethylene. *Green Chem.* **22**, 6540–6546 (2020).
20. Dasireddy, V. D., Štefančič, N. S., Huš, M. & Likozar, B. Effect of alkaline earth metal oxide (MO) $Cu/MO/Al_2O_3$ catalysts on methanol synthesis activity and selectivity via CO_2 reduction. *Fuel* **233**, 103–112 (2018).
21. Peternele, W. S. et al. Experimental investigation of the coprecipitation method: an approach to obtain magnetite and maghemite nanoparticles with improved properties. *J. Nanomater.* **2014**, 682985 (2014).
22. Dinh, C.-T. et al. CO_2 electroreduction to ethylene via hydroxide-mediated copper catalysis at an abrupt interface. *Science* **360**, 783–787 (2018).
23. Liang, Z.-Q. et al. Copper-on-nitride enhances the stable electrosynthesis of multi-carbon products from CO_2. *Nat. Commun.* **9**, 3828 (2018).
24. Lv, J. J. et al. A highly porous copper electrocatalyst for carbon dioxide reduction. *Adv. Mater.* **30**, 1803111 (2018).
25. Karapinar, D. et al. Electroreduction of CO_2 on single-site copper-nitrogen-doped carbon material: selective formation of ethanol and reversible restructuration of the metal sites. *Angew. Chem. Int. Ed.* **58**, 15098–15103 (2019).
26. Li, J. et al. Copper adparticle enabled selective electrosynthesis of n-propanol. *Nat. Commun.* **9**, 4614 (2018).
27. van Deelen, T. W., Mejía, C. H. & de Jong, K. P. Control of metal–support interactions in heterogeneous catalysts to enhance activity and selectivity. *Nat. Catal.* **2**, 955–970 (2019).
28. Pacchioni, G. & Freund, H.-J. Controlling the charge state of supported nanoparticles in catalysis: lessons from model systems. *Chem. Soc. Rev.* **47**, 8474–8502 (2018).
29. Chen, M. & Goodman, D. The structure of catalytically active gold on titania. *Science* **306**, 252–255 (2004).
30. Luches, P. et al. Nature of Ag islands and nanoparticles on the CeO_2(111) surface. *J. Phys. Chem. C* **116**, 1122–1132 (2012).
31. Jiang, S., Klingan, K., Pasquini, C. & Dau, H. New aspects of operando Raman spectroscopy applied to electrochemical CO_2 reduction on Cu foams. *J. Chem. Phys.* **150**, 041718 (2019).
32. Chernyshova, I. V., Somasundaran, P. & Ponnurangam, S. On the origin of the elusive first intermediate of CO_2 electroreduction. *Proc. Natl Acad. Sci. USA* **115**, E9261–E9270 (2018).
33. Chen, X. et al. Controlling speciation during CO_2 reduction on Cu-alloy electrodes. *ACS Catal.* **10**, 672–682 (2019).
34. An, H. et al. Sub-second time-resolved surface enhanced Raman spectroscopy reveals dynamic CO intermediates during electrochemical CO_2 reduction on copper. *Angew. Chem. Int. Ed.* **60**, 16576–16584 (2021).
35. Devasia, D., Wilson, A. J., Heo, J., Mohan, V. & Jain, P. K. A rich catalog of C–C bonded species formed in CO_2 reduction on a plasmonic photocatalyst. *Nat. Commun.* **12**, 2612 (2021).
36. Sander, T. et al. Correlation of intrinsic point defects and the Raman modes of cuprous oxide. *Phys. Rev. B* **90**, 045203 (2014).
37. Mayer, S. T. & Muller, R. H. An in situ Raman spectroscopy study of the anodic oxidation of copper in alkaline media. *J. Electrochem. Soc.* **139**, 426 (1992).
38. Wang, Y. & Pierson, J. Binary copper oxides as photovoltaic absorbers: recent progress in materials and applications. *J. Phys. D* **54**, 263002 (2021).
39. Debbichi, L., Marco de Lucas, M., Pierson, J. & Kruger, P. Vibrational properties of CuO and Cu_4O_3 from first-principles calculations, and Raman and infrared spectroscopy. *J. Phys. Chem. C* **116**, 10232–10237 (2012).
40. Graciani, J. et al. Highly active copper-ceria and copper-ceria-titania catalysts for methanol synthesis from CO_2. *Science* **345**, 546–550 (2014).
41. Kattel, S., Ramírez, P. J., Chen, J. G., Rodriguez, J. A. & Liu, P. Active sites for CO_2 hydrogenation to methanol on Cu/ZnO catalysts. *Science* **355**, 1296–1299 (2017).
42. Yan, B. et al. Tuning CO_2 hydrogenation selectivity via metal-oxide interfacial sites. *J. Catal.* **374**, 60–71 (2019).
43. Kattel, S. et al. CO_2 hydrogenation over oxide-supported PtCo catalysts: the role of the oxide support in determining the product selectivity. *Angew. Chem. Int. Ed.* **55**, 7968–7973 (2016).
44. Kattel, S., Yan, B., Yang, Y., Chen, J. G. & Liu, P. Optimizing binding energies of key intermediates for CO_2 hydrogenation to methanol over oxide-supported copper. *J. Am. Chem. Soc.* **138**, 12440–12450 (2016).
45. Cao, A., Wang, Z., Li, H., Elnabawy, A. O. & Nørskov, J. K. New insights on CO and CO_2 hydrogenation for methanol synthesis: the key role of adsorbate–adsorbate interactions on Cu and the highly active MgO–Cu interface. *J. Catal.* **400**, 325–331 (2021).
46. Xiao, H., Cheng, T. & Goddard, W. A. III Atomistic mechanisms underlying selectivities in C1 and C2 products from electrochemical reduction of CO on Cu(111). *J. Am. Chem. Soc.* **139**, 130–136 (2017).

47. Cheng, T., Xiao, H. & Goddard, W. A. III Full atomistic reaction mechanism with kinetics for CO reduction on Cu(100) from ab initio molecular dynamics free-energy calculations at 298 K. *Proc. Natl Acad. Sci. USA* **114**, 1795–1800 (2017).
48. Luo, M. & Koper, M. A kinetic descriptor for the electrolyte effect on the oxygen reduction kinetics on Pt(111). *Nat. Catal.* **5**, 615–623 (2022).
49. Monteiro, M. C. et al. Absence of CO_2 electroreduction on copper, gold and silver electrodes without metal cations in solution. *Nat. Catal.* **4**, 654–662 (2021).
50. Kresse, G. & Hafner, J. Ab initio molecular dynamics for liquid metals. *Phys. Rev. B* **47**, 558 (1993).
51. Kresse, G. & Furthmüller, J. Efficiency of ab-initio total energy calculations for metals and semiconductors using a plane-wave basis set. *Comput. Mater. Sci.* **6**, 15–50 (1996).
52. Li, J. et al. Enhanced multi-carbon alcohol electroproduction from CO via modulated hydrogen adsorption. *Nat. Commun.* **11**, 3685 (2020).
53. Perdew, J. P., Burke, K. & Ernzerhof, M. Generalized gradient approximation made simple. *Phys. Rev. Lett.* **77**, 3865 (1996).
54. Kresse, G. & Joubert, D. From ultrasoft pseudopotentials to the projector augmented-wave method. *Phys. Rev. B* **59**, 1758 (1999).
55. Nørskov, J. K. et al. Origin of the overpotential for oxygen reduction at a fuel-cell cathode. *J. Phys. Chem. B* **108**, 17886–17892 (2004).
56. Mathew, K., Sundararaman, R., Letchworth-Weaver, K., Arias, T. & Hennig, R. G. Implicit solvation model for density-functional study of nanocrystal surfaces and reaction pathways. *J. Chem. Phys.* **140**, 084106 (2014).
57. Mathew, K., Kolluru, V. C., Mula, S., Steinmann, S. N. & Hennig, R. G. Implicit self-consistent electrolyte model in plane-wave density-functional theory. *J. Chem. Phys.* **151**, 234101 (2019).
58. Jinnouchi, R. & Anderson, A. B. Aqueous and surface redox potentials from self-consistently determined Gibbs energies. *J. Phys. Chem. C* **112**, 8747–8750 (2008).
59. Henkelman, G., Arnaldsson, A. & Jónsson, H. A fast and robust algorithm for Bader decomposition of charge density. *Comput. Mater. Sci.* **36**, 354–360 (2006).

Acknowledgements

This work was financially supported by Suncor Energy, the Natural Sciences and Engineering Research Council (NSERC) of Canada and the CIFAR Bio-Inspired Solar Energy program. S.-F.H. acknowledges support from the Ministry of Science and Technology, Taiwan (contract nos MOST 110-2113-M-009-007-MY2, MOST 110-2628-M-A49-002 and MOST 111-2628-M-A49-007) and from the Yushan Young Scholar Program, Ministry of Education, Taiwan. This research used the synchrotron resources of the Advanced Photon Source (APS), an Office of Science User Facility operated for the US Department of Energy (DOE) Office of Science by Argonne National Laboratory, and was supported by the US DOE under contract no. DE-AC02-06CH11357. The authors thank T. Wu and G. Sterbinsky for technical support at the 9BM beamline of the APS. All DFT computations were performed on the Niflheim supercomputer at the Department of Physics, Technical University of Denmark.

Author contributions

E.H.S. supervised the project. A.X. designed and carried out the experiments and some of the DFT calculations, analysed the data and wrote the paper. S.-F.H., F.L. and J.A. performed the synchrotron X-ray spectroscopy measurements. A.C., Zhenbin Wang and N.K. contributed to the DFT calculations and data analysis. J.E.H. and Y.Y. contributed to the in situ Raman measurements. Y.Y. conducted SEM and TEM characterizations. A.S.R. carried out XPS measurements. A.O. worked on substrate design. F.-Y.W., Z.-Y.L., H.-J.T. and T.-J.L. contributed to performance repeating. The other authors contributed to the preparation of the manuscript.

Competing interests

The authors declare no competing interests.

Additional information

Supplementary information The online version contains supplementary material available at https://doi.org/10.1038/s41929-022-00880-6.

Correspondence and requests for materials should be addressed to Chaofang Dong or Edward H. Sargent.

Peer review information *Nature Catalysis* thanks the anonymous reviewers for their contribution to the peer review of this work.